Key Points:
- Variations in shallow crustal permeability structure at different hydrothermal fields
- Phase lag differences observed at Lucky Strike Hydrothermal Field can be explained as a variation in layer 2A thickness
- The phase lag is sensitive to shallow crustal permeability

Supporting Information:
- Captions for Figure S1 and Table S1
- Figure S1
- Table S1
- Table S2
- Table S3

Correspondence to:
T. Barreyre,
tbarreyre@whoi.edu

Poroelastic response of mid-ocean ridge hydrothermal systems to ocean tidal loading: Implications for shallow permeability structure

Thibaut Barreyre[1] and Robert A. Sohn[1]

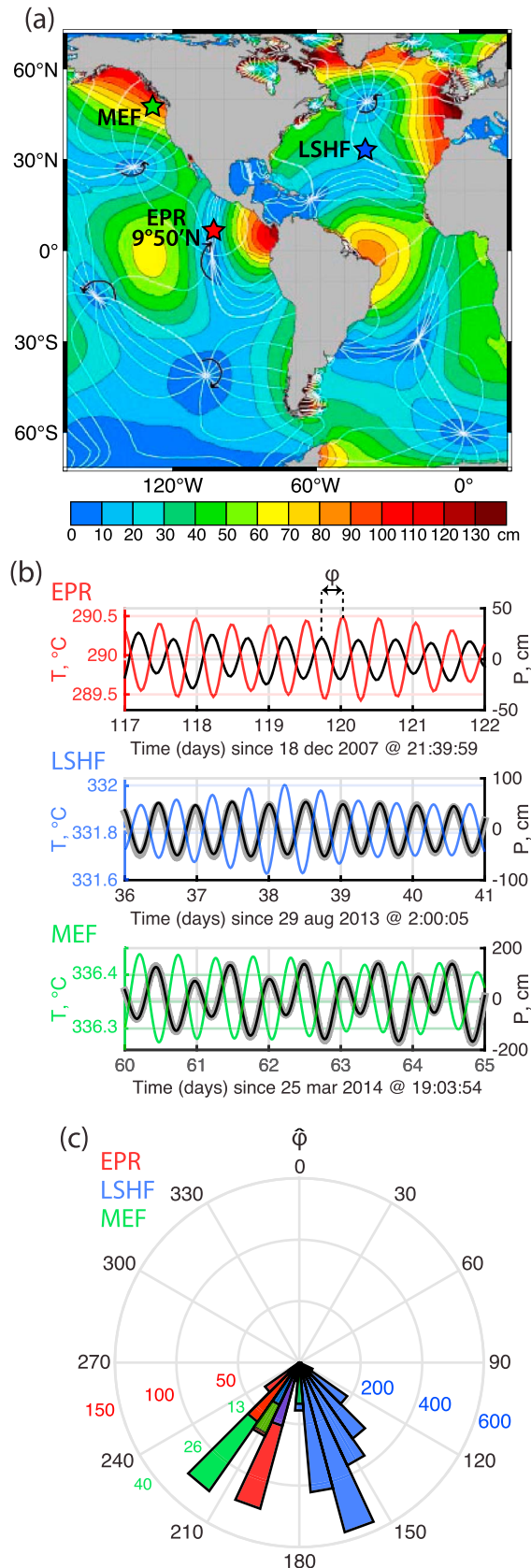[1]Woods Hole Oceanographic Institution, Woods Hole, Massachusetts, USA

Abstract We use the time delay between tidal loading and exit-fluid temperature response for hydrothermal vents to model the poroelastic behavior and shallow upflow zone (SUZ) effective permeability structure of three mid-ocean ridge (MOR) sites with different spreading rates. Hydrothermal vents at Lucky Strike field exhibit relatively small phase lags corresponding to high SUZ effective permeabilities of $\geq \sim 10^{-10}$ m^2, with variations that we interpret as resulting from differences in the extrusive layer thickness. By contrast, vents at East Pacific Rise site exhibit relatively large phase lags corresponding to low SUZ effective permeabilities of $\leq \sim 10^{-13}$ m^2. Vents at Main Endeavour field exhibit both high and low phase lags, suggestive of a transitional behavior. Our results demonstrate that tidal forcing perturbs hydrothermal flow across the global MOR system, even in places where the tidal amplitude is very low, and that the flow response can be used to constrain variations in SUZ permeability structure beneath individual vent fields.

1. Introduction

The response of deep-sea hydrothermal systems to ocean tidal loading is governed by the equations of poroelasticity, which describe the response of a fluid-filled porous medium to applied stress [*Biot*, 1941; *Rice and Cleary*, 1976; *Van der Kamp and Gale*, 1983; *Kümpel*, 1991; *Wang*, 2000]. When a porous medium is loaded, the resultant stress is borne partly by the solid matrix and partly by the interstitial fluid. The cyclical pore fluid pressure perturbation drives interstitial fluid flow at the forcing period, producing a phase lag between the tidal loading signal and the velocity and temperature of the hydrothermal exit-fluids. The magnitude of these phase lags depends upon the system's poroelastic parameters and the upflow zone effective permeability [e.g., *Wang and Davis*, 1996; *Wilcock and McNabb*, 1996; *Jupp and Schultz*, 2004; *Crone and Wilcock*, 2005; *Crone et al.*, 2011]. By quantifying these phase lags we can constrain the upflow zone effective permeability $\left(k_{eff}^{up}\right)$ of young oceanic crust at hydrothermal sites where the exit-fluid velocity and/or temperature have been monitored over sufficiently long periods (e.g., large numbers of tidal cycles) [e.g., *Barreyre et al.*, 2014b].

Over the past two decades, studies at hydrothermal "focus" sites as part of both national and international MOR programs (e.g., RIDGE, Ridge2000, MoMAR, and InterRidge) have generated a large database of exit-fluid temperature records [e.g., *Fornari et al.*, 1998; *Kinoshita et al.*, 1998; *Tivey et al.*, 2002; *Scheirer et al.*, 2006; *Sohn*, 2007; *Larson et al.*, 2007, 2009; *Barreyre et al.*, 2014a]. However, this valuable database has not been systematically analyzed to assess how vent fields hosted in different geological and oceanographic settings respond to tidal loading. Initial results from the Lucky Strike Hydrothermal Field (LSHF) [*Barreyre et al.*, 2014b] demonstrated that tidal loading can perturb the velocity and temperature of high-temperature exit-fluids (Figure 1). However, the applicability of the LSHF results to other vent fields located in different volcanic/tectonic settings and subject to tidal forcing of varying amplitudes has not been established.

In this study, we analyze high-temperature (i.e., black smoker) hydrothermal time-series records from long-term monitoring experiments at the LSHF, located on the slow-spreading Mid-Atlantic Ridge at 37°17′N, the Main Endeavour Field (MEF), located on the intermediate-spreading Juan de Fuca Ridge at 47°57′N, and the hydrothermal field located on the fast-spreading East Pacific Rise (EPR) at 9°50′N (Figure 1a). We find that most temperature records, regardless of geological or oceanographic setting, exhibit variability at both semidiurnal and diurnal tidal periods, with the strongest signal at the principal semidiurnal periods (M2, S2, N2, and K2). Cross-spectral analyses reveal robust phase relationships between exit-fluid temperature and tidal forcing for a subset of these data, which allows us to constrain and compare the shallow upflow zone (SUZ) effective permeability of vent fields from three different MORs, including structural variations within individual sites.

Figure 1. (a) The M2 tidal constituent. Amplitude (cm) is indicated by color, and the white lines are cotidal differing by 1 h. The curved arrows around the amphidromic points show the direction of the tides, each indicating a synchronized 6 h period. Modified from R. D. Ray's GSFC-NASA map (see references at *Ray* [2015]). The main hydrothermal fields concerned in this study are indicated by colored stars: Lucky Strike Hydrothermal Field (LSHF), Main Endeavour Field (MEF), and East Pacific Rise at 9°50′N (EPR 9°50′N). Note the proximity of EPR 9°50′N field to an amphidromic point. (b) Example of tidal signature (i.e., filtered temperature signal) illustrated over a 5 day time window on high-temperature record at EPR (red), LSHF (blue), and MEF (green), and the corresponding variations in modeled bottom pressure (black) and real bottom pressure data when available (gray). (c) Rose diagram displaying the estimated phase lag between tidal loading and exit-fluid temperature ($\hat{\varphi}$, °) at the M2 period for 60 day windows with coherency ($\gamma^2 \geq 0.85$) for EPR (red), LSHF (blue), and MEF (green).

2. Data Set

For our analyses we mined the complete set of publicly available (Marine Geoscience Data System, PANGAEA, European Multidisciplinary Seafloor and water column Observatory, and Ocean Networks Canada) exit-fluid temperature data for vents at the LSHF, MEF, and EPR sites [e. g., *Fornari et al.*, 1998; *Tivey et al.*, 2002; *Scheirer et al.*, 2006; *Larson et al.*, 2009; *Barreyre et al.*, 2014a].

The data acquired come from four sets of instruments, which were used to monitor hydrothermal outflow high-temperature: the MISO high-temperature probes (at EPR and LSHF) [*Fornari et al.*, 1998], the NKE S2T6000 high-temperature probes (at LSHF) [*Barreyre et al.*, 2014a], the resistivity-temperature probe (at MEF-S&M) [*Larson et al.*, 2007], and the benthic and resistivity sensors (BARS at MEF-Grotto) (user's manual for *Lilley* [2010]). The instrument-independent consistency of temperature measurements (i.e., repeatability) was assured by both factory and laboratory calibrations.

We examined a total of 232 records, corresponding to ~157 record-years of data, and performed quality control by removing time windows with data gaps, glitches or inconsistencies and records exhibiting low exit-fluid temperatures (<200°C, thought to correspond to probes with data that are not representative of the true effluent temperature because they were either dislodged or became insulated from the flow). The remaining

Table 1. Average Phase Lag $\left(\hat{\varphi}_a\right)$ and Errors $\left(\bar{e}_{\hat{\varphi}_a}\right)$ Estimates at M_2 Semidiurnal Frequency and Average Effective Permeability of the Upflow Zone $\left(\bar{k}_{\text{eff}}^{\text{up}}\right)$ Constrained From 1-D Analytical Poroelastic Model for H = Depth to the Layer 2A/2B (H_{2A})

Hydrothermal fields		$\hat{\varphi}_a(°)$	$\bar{e}_{\hat{\varphi}_a}(°)$	H_{2A} (m)	$\bar{k}_{\text{eff}}^{\text{up}}$ (m^2)
LSHF(MAR)	West	155	5	300/600[a]	~$3*10^{-10}$/~$6*10^{-10}$
	East	173	4	600[a]	~$3*10^{-10}$
MEF(JdFR)	North	217	2.5	460[b]	~$2.5*10^{-13}$
	South	178.5	1.5		~$2*10^{-10}$
9°50′N(EPR)	L-Vent	207	5	155[c]	~$5*10^{-14}$

[a]*Arnulf et al.* [2011].
[b]*Van Ark et al.* [2007].
[c]*Sohn et al.* [2004].

total of 206 records (111 record-years of data) constitutes a high-quality catalog of "cleaned" records that are free of known instrumentation errors. These records have highly variable lengths (days to ~2 years), sampling frequencies (4 s to 288 min), resolutions (~0.025°C to ~1.2°C), and data densities (104 records, ~49 years of recording for EPR-9°50′N; 92 records, ~60 years of recording for LSHF; and 10 records, ~2.3 years of recording for MEF)-Table S1 in the supporting information. Contemporaneous measurements of the tidal loading signal at the observatory sites are limited, so for consistency we compare the exit-fluid high-temperature records to bottom pressure time-series data generated with the GOT4.7 model [*Ray*, 2013]. Comparison of the model data to bottom pressure measurements, when available (e.g., Figure 1b), validates this approach by demonstrating that the phase of the model data is accurate to within 0.001°, which is much smaller than the accuracy of the phase lag estimates, as we describe below.

3. Results and Discussion

3.1. Phase Lags Between Tidal Forcing and Exit-Fluid Thermal Response

We estimated the coherency and phase lag between the cleaned exit-fluid high-temperature record catalog and the tidal loading data by applying multitaper [*Thomson*, 1982] cross-spectral methods with adaptive weighting [*Percival and Walden*, 1993] to sliding time windows. We used a range of time windows (30, 60, and 90 days) and time bandwidth products (NW = 3, 7/2, and 4) and found that a 60 day window with NW = 4 provided the best trade-off between temporal resolution and phase estimate stability given the range of sample intervals and record lengths found in the data. Phase lag uncertainties are estimated by jackknifing the independent Fourier coefficients obtained for the set of orthogonal tapers generated by the multitaper method [*Efron and Stein*, 1981] (average uncertainty values are given in Table 1 and more details in Tables S1 and S3). Removal of records shorter than 60 days resulted in a final data set for cross-spectral analyses comprising 69 records (~47.8 years of recording) for the EPR-9°50′N vents, 70 records (~58.4 years of recording) for the LSHF vents, and 5 records (~1.4 years of recording) for the MEF vents.

Exit-fluid temperature is coherent with bottom pressure in high-temperature records from all three sites at both semidiurnal (M2, S2, N2, and K2; Figures 2 and S1) and diurnal (K1 and O1-except at LSHF) periods, but the phase lag estimates do not stabilize until the coherency between tidal loading and exit-fluid temperature is ≥ ~0.85. Variability in the coherency and phase lag estimates is caused by noise in the exit-fluid temperature data and the fact that the temperature data can be also influenced by bottom currents at tidal periods [*Tivey et al.*, 2002]. To minimize the impact of this variability and maximize the signal-to-noise ratio, we restricted our phase angle analysis to time windows with a coherency (γ^2) ≥ 0.85 at the M2 frequency. Furthermore, for data records acquired contemporaneously in the same housing (as is common in many deployments [*Fornari et al.*, 1994, 1996, 1998; *Barreyre et al.*, 2014a]), we only used the record with the highest coherency to tidal pressure (at M2 frequency). After applying these stringent criteria for phase analysis, our final data set for poroelastic modeling consists of two records (287 60-day windows, ~2.4 years of recording) for the EPR-9°50′N, 30 records (2536 60-day windows, ~27 years of recording) for the LSHF, and two records (60 60-day windows, ~0.8 years of recording) for the MEF (Figures 1c and 2). These highly coherent records exhibit stable phase lag estimates at the M2 frequency, ~90% of which fall within the 135°–225° range predicted by poroelastic theory [*Jupp and Schultz*, 2004; *Crone and Wilcock*, 2005]
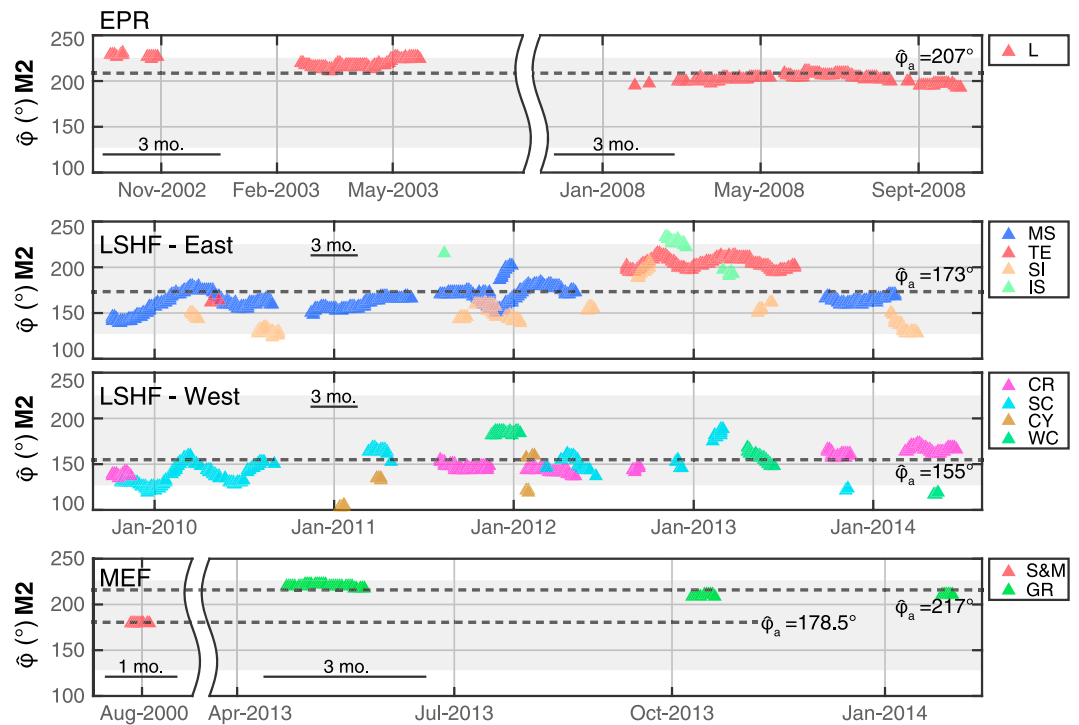
Figure 2. Temporal variation of the estimated phase lag between tidal loading and exit-fluid temperature ($\hat{\varphi}$, °) at the M2 period for EPR (first panel), LSHF (second and third panels) and MEF (fourth panel). Average values are listed and shown by dashed horizontal black lines. Colors indicate the different vents within individual hydrothermal fields. Note that time scales are different for the various panels, but 3-month and 1-month time scale bars are shown for comparative purposes.

(gray band on Figure 2), corresponding to lower outflow temperatures during high tide and higher temperatures during low tide.

We find that phase lag estimates for individual vents vary smoothly about an average value over the recording intervals (Figure 2), and we take these average values to represent the nominal phase lag with respect to tidal loading for each vent. The smooth, periodic (~6 months) variations around these average values are identical for all of the semidiurnal frequencies (Figure S1), indicating that they are not random. These systematic variations are likely associated with oceanographic effects (e.g., bottom currents), and in principle they can be removed from the data if contemporaneous bottom current measurements are available. However, current measurements are only available for a small subset of the existing data, meaning that additional research will be required to establish systematic relationships between bottom currents and exit-fluid temperature.

We find significant differences in the average phase lag estimates from the various vent fields sampled in our study. The largest phase lag averages are observed for L vent on the EPR (207°) and S&M vent on the JdFR (217°). The smallest phase lags are observed at the LSHF, where there also appears to be a difference between vents located on the west (155°) versus the east (173°) side of the field. Intrasite variability is also evident at the MEF, where the Grotto site exhibits lags of 178°, which is ~40° less than the S&M site. These differences are much larger than the phase lag uncertainties and intersite variability, indicating that they arise from deterministic differences in the subsurface permeability structure.

Our final data set for poroelastic modeling constitutes ~19% of the available exit-fluid temperature data from the three study sites. This small percentage is primarily due to (1) the intrinsic difficulty of obtaining accurate fluid temperature records from deep-sea vents and (2) the relatively poor resolution (e.g., 1.2 °C at EPR) of many of the temperature probes that have been deployed in the past. Poor measurement resolution precludes capturing the thermal response to tidal loading when the tidal amplitude is small (e.g., at EPR, which is near an amphidromic point). These considerations highlight the need to develop high-resolution probes and improved deployment/measurement techniques to enhance the data quality for instruments being used at seafloor observatory sites in the future.
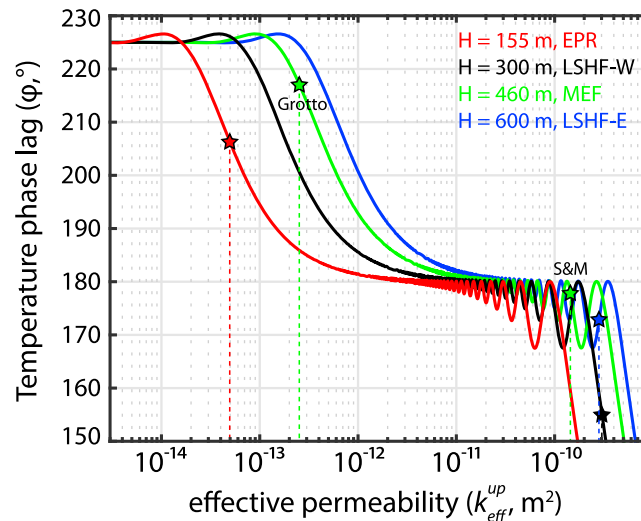
Figure 3. Predicted phase lag of exit-fluid discharge temperature $(\varphi, °)$ behind the ocean tide as a function of effective permeability of the upflow zone $\left(k_{\text{eff}}^{\text{up}}, m^2\right)$. For consistency, we run the different model cases using the same poroelastic and fluid parameters (i.e., using the ones of LSHF, Table S2), but the depth of the impermeable boundary layer, H, changes according to constraints from seismic data for each site (Tables 1 and S3). Average estimated phase lags $(\hat{\varphi}_a)$ for the different fields (Tables 1 and S3) are shown by stars.

3.2. Constraints on Effective Permeability of the Upflow Zone

Following the same methodology described by *Barreyre et al.* [2014b], we use the highly coherent $(\gamma^2 \geq 0.85)$ phase lags in conjunction with the one-dimensional model of *Jupp and Schultz* [2004] to constrain poroelastic parameters (e.g., permeability) at the LSHF-E, LSHF-W, EPR-L, MEF-S&M, and MEF-Grotto vent sites. For consistency, we use the same baseline modeling parameters (i.e., storage compressibility, porosity, bulk density, grain bulk modulus, fluid bulk modulus, and matrix-drained-modulus) for all three sites (see Table S2) [*Crone and Wilcock*, 2005; *Barreyre et al.*, 2014b and references therein]. We allow for small variations in fluid density according to the oceanographic setting (depth and temperature) of each site, but the most important difference between the sites is their lithostratigraphy.

In a single-layer model, the depth of the boundary that arrests the downward propagation of the tidally induced pressure gradient (i.e., the thickness of the permeable layer, H) is a key parameter. For basalt-hosted vent fields, there are two primary lithographic interfaces where the permeability changes significantly: the extrusive/intrusive boundary (i.e., seismic layer 2A/2B) and the intrusive/cumulate boundary (i.e., seismic layer 2B/2C = magma chamber depth). These interface depths have been constrained by seismic studies for the three study sites [e.g., *Detrick et al.*, 1987; *Sohn et al.*, 2004; *Singh et al.*, 2006; *Van Ark et al.*, 2007; *Arnulf et al.*, 2011, 2014; *Crawford et al.*, 2013], which provides a template for our models (Tables 1 and S3). We do not know, a priori, the propagation depth for the tidal loading pressure signal, so the model was run with two different values for the permeable layer thickness, H, at each site: (1) $H=$ depth to the layer 2A/2B interface and (2) $H=$ depth to the axial magma lens. We found that these different assumptions for H do not change the order of magnitude of the crustal upflow zone permeability required to fit the phase lag data (Tables 1 and S3). Given that the permeability estimates required to fit the phase lag data vary by several orders of magnitude (Figures 3 and 4), we show that the poroelastic response to tidal loading is primarily controlled by the permeability of the upflow zone just beneath the seafloor (i.e., layer 2A).

At the EPR, where the base of layer 2A is located at the relatively shallow depth of ~155 mbsf [*Sohn et al.*, 2004], the relatively large phase lag estimate for L vent (207° ± 5°) requires a SUZ effective permeability of ~5 × 10⁻¹⁴ m². By contrast, at the LSHF the relatively small phase lags (155° ± 5° at LSHF-W and 173° ± 4° at LSHF-E) require a much higher SUZ effective permeability for layer 2A of ~3 × 10⁻¹⁰ m². The different phase lags estimated for the west versus east vents at the LSHF are consistent with variations in the extrusive layer thickness observed in seismic data (300 m for the west vents versus 600 m for the east vents) [*Arnulf et al.*, 2011, 2014],
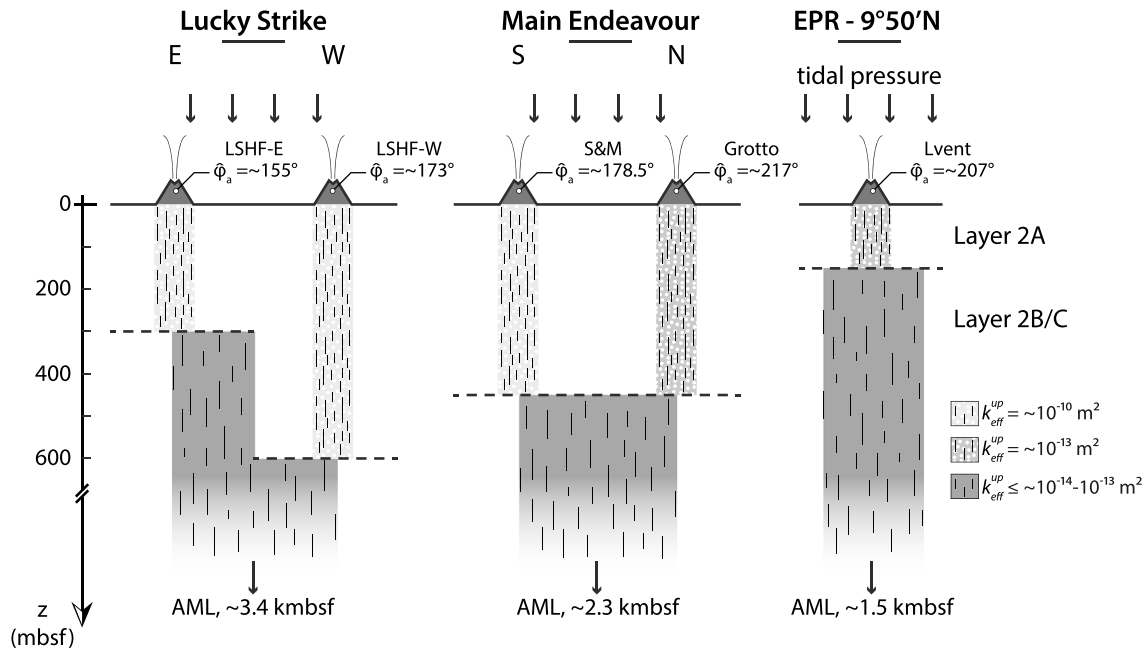
Figure 4. Schematic model of the shallow upflow zone permeability structure $\left(k_{\mathrm{eff}}^{\mathrm{up}}\right)$ beneath the hydrothermal fields at each site required to fit the phase lag data.

although we cannot rule out permeability variations on the basis of our data alone. Transitional behaviors are observed at the MEF where the extrusive layer thickness is ~450 m [*Van Ark et al.*, 2007]. For Grotto vent, the phase lag of $217° \pm 2.5°$ requires a SUZ effective permeability of $\sim 2.5 \times 10^{-13}$ m^2 for layer 2A, whereas the smaller phase lag observed for S&M vent ($178.5° \pm 1.5°$) requires a SUZ effective permeability estimate of $\sim 2 \times 10^{-10}$ m^2. Since the seismic data indicate the extrusive layer thickness is the same for both of these vents [*Van Ark et al.*, 2007], at the MEF the phase lag difference between the two sites appears to result from a variation in SUZ effective permeability rather than 2A layer thickness. Magnetics data indicate that the S&M and Grotto vents, which are separated by a distance of ~150 m, are fed by distinct fluid upwelling zones [*Tivey and Johnson*, 2002], and our results suggest these zones have different SUZ effective permeabilities. However, this interpretation is tentative because the phase lag estimate for the S&M vent is based on a fairly small data window (~69 days).

Overall, we model the shallow crust beneath vents with phase lags greater than 200° with a low-permeability ($k_{\mathrm{eff}}^{\mathrm{up}} \sim 10^{-13}$–$10^{-14}$ m^2) layer, and the shallow crust beneath vents with phase lags less than 180° with a relatively high-permeability ($k_{\mathrm{eff}}^{\mathrm{up}} \sim 10^{-10}$ m^2) layer. This dichotomy arises from the sensitivity of the phase lag to the SUZ effective permeability (Figure 3). If the extrusive layer upflow zone effective permeability is $< \sim 10^{-11}$ m^2, the temperature signal will lag the tidal loading signal by $> 180°$, but if the extrusive layer upflow zone effective permeability is $> \sim 10^{-11}$ m^2, then the phase lag will be $< 180°$. This basic result is relatively insensitive to the permeable layer thickness, H, suggesting that phase lag estimates may provide a simple way to discern between low- versus high-upflow zone effective permeability extrusive layers at deep-sea hydrothermal vent fields. To test this hypothesis, however, it will be necessary to develop multilayer poroelastic models capable of incorporating more realistic lithostratigraphies with multiple interfaces.

To first order, the upflow zone effective permeability of the extrusive layer depends on the local tectono-magmatic history. At the slow-spreading ridges, such as the LSHF, the extrusive layer is relatively thick [*Smith and Cann*, 1993; *Cannat*, 1996; *Hooft et al.*, 2000; *Hussenoeder et al.*, 2002] and is tectonized by faults and fissures formed by spreading in-between relatively rare magmatic events, which provides permeable pathways for ascending fluids. In contrast, at fast-spreading ridges, such as the EPR, the extrusive layer is relatively thin and the seafloor is repaved by frequent volcanic activity [e.g., *Fornari et al.*, 2004, 2012], which hinders the formation of high-permeability upflow zones. This contrast in tectonomagmatic history provides the simplest explanation for the differences in phase lag that we observe, and the SUZ effective permeability structures that we infer, between the LSHF and the EPR vent fields. Our results from the intermediate-spreading JdFR are more enigmatic and

suggest that processes related to hydrothermal alteration and mineralization can affect the crustal upflow zone permeability immediately beneath a vent field and produce strong, localized gradients in permeability.

Our permeability estimates ($\sim 10^{-13}$ to 10^{-10} m^2) are broadly consistent with estimates derived for basalt-hosted, MOR hydrothermal fields via other methods. Our estimates fall within the range of permeabilities estimated for upper crust from borehole flow calculations ($\sim 10^{-9}$–10^{-14} m^2) [*Becker and Davis*, 2004, and references therein], with in situ permeability tests in shallow submarine wellbores (as large as 10^{-11} m^2) [*Fisher*, 1998], with permeability estimates from sedimented ridge flanks ($\sim 10^{-10}$ m^2) [*Davis et al.*, 2000], with estimates from pressure diffusion along the borehole transects (10^{-9}–10^{-10} m^2) [*Davis et al.*, 2001], with permeabilities inferred from large-scale numerical models of fluid flow and heat transport (10^{-11} to 10^{-9} m^2) [e.g., *Stein and Fisher*, 2003], and with estimates for layer 2A of Endeavour segment inferred from seafloor fissuring ($\sim 10^{-10}$ to 10^{-11} m^2) [*Hearn et al.*, 2013]. These permeability estimates are also similar to those obtained for shallow subaerial Hawaiian basalts (10^{-11} to 10^{-9} m^2) [*Ingebritsen and Scholl*, 1993].

Another important outcome of our study is that MOR vent fields are sensitive to even small levels of ocean tidal loading (e.g., ~ 40–50 cm at the EPR compared to ~ 200 cm at the MEF), suggesting that careful monitoring (i.e., high-resolution, high-precision, and high sampling frequency) of exit-fluid temperatures over long periods of time has the potential to constrain SUZ effective permeability at vent fields essentially anywhere on the global MOR system. Our results emphasize the importance of obtaining long-term records from deep-sea hydrothermal systems in order to obtain robust statistical results, given the high-levels of noise associated with exit-fluid temperature data (e.g., previous analyses using more temporally and spatially limited data from similar instruments failed to find a relationship between tidal pressure and high-temperature exit-fluids at the EPR [*Scheirer et al.*, 2006]); suggesting that contemporaneous measurements of bottom currents may be important for understanding the role that currents play in modulating fluid temperatures at tidal periods. Finally, while our results indicate that the shallow crust exerts a primary control on the poroelastic response to tidal loading, it is nevertheless clear that poroelastic models incorporating multiple permeable layers, supplemented by high-resolution geophysical surveys, are needed to accurately determine the volcanic stratigraphy underlying deep-sea vent fields and model the crustal response to tidal loading.

4. Conclusions

We have estimated the phase lag between tidal pressure and exit-fluid temperature for high-temperature ($T > 200°C$) vents at three deep-sea hydrothermal fields (LSHF, EPR, and MEF) and then used this information to constrain SUZ effective permeability in a homogeneous, single-layer, analytical poroelastic model. Our principal conclusions are as follows:

1. The various vent fields in our study exhibit statistically significant phase lags that correspond to variations in shallow crustal permeability structure. Vent sites at the slow-spreading LSHF exhibit relatively small phase lags corresponding to relatively high layer 2A SUZ effective permeabilities of $> \sim 10^{-10}$ m^2. By contrast, vent sites at the fast-spreading EPR exhibit relatively large phase lags corresponding to relatively low layer 2A SUZ effective permeabilities of $< \sim 10^{-13}$ m^2. Vent sites at the intermediate-spreading JdFR exhibit both of these behaviors, but the available data are more limited.

2. Systematic phase lag differences are observed between vent sites hosted on the east versus west side of the LSHF, which can be explained as a variation in layer 2A thickness. Phase lag differences between the S&M and Grotto vent sites on the JdFR are tentatively interpreted as variations in shallow crustal permeability related to hydrothermal alteration and mineralization.

3. The phase lag between tidal pressure and exit-fluid temperature is sensitive to shallow crustal permeability (i.e., layer 2A) with a relatively sharp transition at a value of $\sim 180°$ from high-permeability systems ($\phi < 180°$, $k_{eff}^{up} > \sim 10^{-11}$ m^2) to low-permeability systems ($\phi > 180°$, $k_{eff}^{up} < \sim 10^{-11}$ m^2). This result needs to be refined by developing analytical solutions for poroelastic systems with multiple permeable layers.

References

Arnulf, A. F., S. C. Singh, A. J. Harding, G. M. Kent, and W. Crawford (2011), Strong seismic heterogeneity in layer 2A near hydrothermal vents at the Mid-Atlantic Ridge, *Geophys. Res. Lett.*, 38, L13320, doi:10.1029/2011GL047753.

Arnulf, A. F., A. J. Harding, S. C. Singh, G. M. Kent, and W. C. Crawford (2014), Nature of upper crust beneath the Lucky Strike volcano using elastic full waveform inversion of streamer data, *Geophys. J. Int.*, 196(3), 1471–1491.

Barreyre, T., J. Escartín, R. Sohn, M. Cannat, V. Ballu, and W. Crawford (2014a), Temporal variability and tidal modulation of hydrothermal exit-fluid temperatures at the Lucky Strike deep-sea vent field, Mid-Atlantic Ridge, *J. Geophys. Res. Solid Earth*, *119*, 2543–2566, doi:10.1002/2013JB010478.

Barreyre, T., J. Escartin, R. Sohn, and M. Cannat (2014b), Permeability of the Lucky Strike deep-sea hydrothermal system: Constraints from the poroelastic response to ocean tidal loading, *Earth Planet. Sci. Lett.*, *408*, 146–154.

Becker, K., and E. Davis (2004), In situ determinations of the permeability of the igneous oceanic crust, in *Hydrogeology of the Oceanic Lithosphere*, edited by E. E. Davis and H. Elderfield, pp. 189–224, Cambridge Univ. Press, Cambridge, U. K.

Biot, M. A. (1941), General theory of three-dimensional consolidation, *J. Appl. Phys.*, *12*, 155–164.

Cannat, M. (1996), How thick is the magmatic crust at slow-spreading oceanic ridges?, *J. Geophys. Res.*, *101*, 2847–2857.

Crawford, W. C., A. Rai, S. C. Singh, M. Cannat, J. Escartin, H. Wang, R. Daniel, and V. Combier (2013), Hydrothermal seismicity beneath the summit of Lucky Strike volcano, Mid-Atlantic Ridge, *Earth Planet. Sci. Lett.*, doi:10.1016/j.epsl.2013.04.028.

Crone, T. J., and S. D. Wilcock (2005), Modeling the effects of tidal loading on mid-ocean ridge hydrothermal systems, *Geochem. Geophys. Geosyst.*, *6*, Q07001, doi:10.1029/2004GC000905.

Crone, T. J., M. Tolstoy, and D. F. Stroup (2011), Permeability structure of young ocean crust from poroelastically triggered earthquakes, *Geophys. Res. Lett.*, *38*, L05305, doi:10.1029/2011GL046820.

Davis, E. E., K. Wang, K. Becker, and R. E. Thomson (2000), Formation-scale hydraulic and mechanical properties of oceanic crust inferred from pore pressure response to periodic seafloor loading, *J. Geophys. Res.*, *105*, 13,423–13,435.

Davis, E. E., K. Wang, R. E. Thomson, K. Becker, and J. F. Cassidy (2001), An episode of seafloor spreading and associated plate deformation inferred from crustal fluid pressure transients, *J. Geophys. Res.*, *106*, 21,953–21,963, doi:10.1029/2000JB000040.

Detrick, R. S., P. Buhl, E. Vera, J. Mutter, J. Orcutt, J. Madsen, and T. Brocher (1987), Multi-channel seismic imaging of a crustal magma chamber along the East Pacific Rise, *Nature*, *326*, 35–41.

Efron, B., and C. Stein (1981), The jackknife estimate of variance, *Ann. Stat.*, *9*(3), 586–596, doi:10.1214/aos/1176345462.

Fisher, A. T. (1998), Permeability within basaltic oceanic crust, *Rev. Geophys.*, *36*, 143–182.

Fornari, D., C. L. Van Dover, T. Shank, R. Lutz, and M. Olsson (1994), A versatile, low-cost temperature sensing device for time-series measurements at deep sea hydrothermal vents, *Bridge Newsl.*, *6*, 37–40.

Fornari, D. J., F. Voegeli, and M. Olsson (1996), Improved low-cost, time-lapse temperature loggers for deep ocean and sea floor observatory monitoring, *Ridge Events*, *7*, 13–16.

Fornari, D. J., T. Shank, K. L. Von Damm, T. K. P. Gregg, M. Lilley, G. Levai, A. Bray, R. M. Haymon, M. R. Perfit, and R. Lutz (1998), Time-series temperature measurements at high-temperature hydrothermal vents, East Pacific Rise 9°49′–51′N: Evidence for monitoring a crustal cracking event, *Earth Planet. Sci. Lett.*, *160*, 419–431.

Fornari, D. J., et al. (2004), Submarine lava flow emplacement at the East Pacific Rise 9°50′N: Implications for uppermost ocean crust stratigraphy and hydrothermal fluid circulation, in *Mid-Ocean Ridges: Hydrothermal Interactions Between the Lithosphere and Oceans*, *Geophys. Monogr. Ser.*, vol. 148, edited by C. R. German, J. Lin, and L. M. Parson, pp. 187–218, AGU, Washington, D. C.

Fornari, D. J., et al. (2012), The East Pacific Rise between 9°N and 10°N: Twenty-five years of integrated, multidisciplinary oceanic spreading center studies, *Oceanography*, *25*(1), 18–43, doi:10.5670/oceanog.2012.02.

Hearn, C. K., K. L. Homola, and H. P. Johnson (2013), Surficial permeability of the axial valley seafloor: Endeavour Segment, Juan de Fuca Ridge, *Geochem. Geophys. Geosyst.*, *14*, 3409–3424, doi:10.1002/ggge.20209.

Hooft, E. E., R. S. Detrick, D. R. Toomey, J. A. Collins, and J. Lin (2000), Crustal thickness and structure along three contrasting spreading segments of the Mid-Atlantic Ridge, 33.5°–35°N, *J. Geophys. Res.*, *105*, 8205–8226.

Hussenoeder, S. A., G. M. Kent, and R. S. Detrick (2002), Upper crustal seismic structure of the slow spreading Mid-Atlantic Ridge, 35 degrees N: Constraints on volcanic emplacement processes, *J. Geophys. Res.*, *107*(B8), 2156, doi:10.1029/2001JB001691.

Ingebritsen, S. E., and M. A. Scholl (1993), The hydrogeology of Kilauea volcano, *Geothermics*, *22*, 255–270.

Jupp, T. E., and A. Schultz (2004), A poroelastic model for the tidal modulation of seafloor hydrothermal systems, *J. Geophys. Res.*, *109*, B03105, doi:10.1029/2003JB002583.

Kinoshita, M., R. P. Von Herzen, O. Matsubayashi, and K. Fujioka (1998), Erratum to 'Tidally-driven effluent detected by long-term temperature monitoring at the TAG hydrothermal mound, Mid-Atlantic Ridge' [Phys. Earth Planet. Int. 108_1998/143–154], *Phys. Earth Planet. Inter.*, *109*, 201–212.

Kümpel, H. J. (1991), Poroelasticity: Parameters reviewed, *Geophys. J. Int.*, *105*(3), 783–799.

Larson, B. I., E. J. Olson, and E. J. Lilley (2007), In situ measurement of dissolved chloride in high temperature hydrothermal fluids, *Geochim. Cosmochim. Acta*, *71*, 2510–2523, doi:10.1016/j.gca.2007.02.013.

Larson, B. I., M. D. Lilley, and E. J. Olson (2009), Parameters of subsurface brines and hydrothermal processes 12–15 months after the 1999 magmatic event at the Main Endeavor Field as inferred from in situ time series measurements of chloride and temperature, *J. Geophys. Res.*, *114*, B01207, doi:10.1029/2008JB005627.

Lilley, M. D. (2010), Benthic and Resistivity Sensors (BARS) user's manual. [Available at file:///Users/tbarreyre/Downloads/BARS-Complete%20with%20page%20numbers.pdf.]

Percival, D., and A. Walden (1993), *Spectral Analysis for Physical Applications*, Cambridge Univ. Press, Cambridge, U. K.

Ray, R. D. (2013), Precise comparisons of bottom-pressure and altimetric ocean tides, *J. Geophys. Res. Oceans*, *118*, 4570–4584, doi:10.1002/jgrc.20336.

Ray, R. D. (2015), TOPEX/Poseidon: Revealing hidden tidal energy, GSFC, NASA. [Available http://marinedataliteracy.org/grids/360_to_180.htm.]

Rice, J. R., and M. P. Cleary (1976), Some basic stress diffusion solutions for fluid-saturated elastic porous media with compressible constituents, *Rev. Geophys.*, *14*, 227–241.

Scheirer, D. S., T. M. Shank, and D. J. Fornari (2006), Temperature variations at diffuse and focused flow hydrothermal vent sites along the northern East Pacific Rise, *Geochem. Geophys. Geosyst.*, *7*, Q03002, doi:10.1029/2005GC001094.

Singh, S. C., W. C. Crawford, H. Carton, T. Seher, V. Combier, M. Cannat, J. P. Canales, D. Dusunur, J. Escartín, and J. M. Miranda (2006), Discovery of a magma chamber and faults beneath a Mid-Atlantic Ridge hydrothermal field, *Nature*, *442*, 1029–1032, doi:10.1038/nature05105.

Smith, D. K., and J. R. Cann (1993), Building the crust at the Mid-Atlantic Ridge, *Nature*, *365*, 707–715.

Sohn, R. A. (2007), Stochastic analysis of exit fluid temperature records from the active TAG hydrothermal mound (Mid-Atlantic Ridge, 26°N): 1. Modes of variability and implications for subsurface flow, *J. Geophys. Res.*, *112*, B07101, doi:10.1029/2006JB004435.

Sohn, R. A., S. C. Webb, and J. A. Hildebrand (2004), Fine-scale seismic structure of the shallow volcanic crust on the East Pacific Rise at 9°50′N, *J. Geophys. Res.*, *109*, B12104, doi:10.1029/2004JB003152.

Stein, J. S., and A. T. Fisher (2003), Observations and models of lateral hydrothermal circulation on young ridge flank: Numerical evaluation of thermal and chemical constraints, *Geochem. Geophys. Geosyst.*, *4*(3), 1026, doi:10.1029/2002GC000415.

Thomson, D. J. (1982), Spectrum estimation and harmonic analysis, *Proc. IEEE*, *70*, 1055–1096.

Tivey, M. A., and H. P. Johnson (2002), Crustal magnetization reveals subsurface structure of Juan de Fuca Ridge hydrothermal vent fields, *Geology*, *30*(11), 979–982.

Tivey, M. K., A. M. Bradley, T. M. Joyce, and D. Kadko (2002), Insights into tide-related variability at seafloor hydrothermal vents from time-series temperature measurements, *Earth Planet. Sci. Lett.*, *202*, 693–707.

Van Ark, E., R. S. Detrick, J. P. Canales, S. M. Carbotte, A. J. Harding, G. M. Kent, M. R. Nedimovic, W. S. D. Wilcock, J. B. Diebold, and J. M. Babcock (2007), Seismic structure of the Endeavour Segment, Juan de Fuca Ridge: Correlations with seismicity and hydrothermal activity, *J. Geophys. Res.*, *112*, B02401, doi:10.1029/2005JB004210.

Van der Kamp, G., and J. E. Gale (1983), Theory of Earth tide and barometric effects in porous formations with compressible grains, *Water Resour. Res.*, *19*, 538–544.

Wang, H. F. (2000), *Theory of Linear Poroelasticity With Applications to Geomechanics and Hydrogeology*, Princeton Univ. Press, Princeton, N. J.

Wang, K., and E. Davis (1996), Theory for the propagation of tidally induced pore pressure variations in layered subseafloor formations, *J. Geophys. Res.*, *101*, 11,483–11,495.

Wilcock, W. S. D., and A. McNabb (1996), Estimates of crustal permeability on the Endeavour segment of the Juan de Fuca mid-ocean ridge, *Earth Planet. Sci. Lett.*, *138*, 83–91.